chemistry

MDPI

Article

Synthesis, Phase Formation, and Raman Spectroscopy of Ni and Zn(Mg) Codoped Bismuth Stibate Pyrochlore

Nadezhda A. Zhuk [1,*], Sergey V. Nekipelov [2], Olga V. Petrova [2], Boris A. Makeev [3], Sergey I. Isaenko [3], Maria G. Krzhizhanovskaya [4], Kristina N. Parshukova [5], Roman I. Korolev [5] and Ruslana A. Simpeleva [5]

[1] Institute of Natural Sciences, Syktyvkar State University, Oktyabrsky Prospect 55, Syktyvkar 167001, Russia
[2] Institute of Physics and Mathematics of the Komi Science Center UB RAS, Oplesnina st. 4, Syktyvkar 167982, Russia; nekipelovsv@mail.ru (S.V.N.); teiou@mail.ru (O.V.P.)
[3] Institute of Geology of the Komi Science Center UB RAS, Pervomaiskaya st. 48, Syktyvkar 167982, Russia; makboris@mail.ru (B.A.M.); s.i.isaenko@gmail.com (S.I.I.)
[4] Institute of Earth Sciences, Saint Petersburg State University, University Emb. 7/9, Saint Petersburg 199034, Russia; krzhizhanovskaya@mail.ru
[5] Institute of Natural Sciences, Saint Petersburg State University, University Emb. 7/9, Saint Petersburg 199034, Russia; kristinaparshukova17@gmail.com (K.N.P.); korolev36a@gmail.com (R.I.K.); rsimpeleva@mail.ru (R.A.S.)
* Correspondence: nzhuck@mail.ru

Abstract

Complex antimony pyrochlores $Bi_{2.7}M_{0.46}Ni_{0.70}Sb_2O_{10+\Delta}$ (M = Zn, Mg) were synthesized from oxide precursors, using the solid-state reaction method. For each composition variant, the pyrochlore phase formation process was studied during solid-state synthesis in the range of 500–1050 °C. The influence of zinc and magnesium on the phase formation process was established. The interaction of oxide precursors occurs at a temperature of 600 °C and higher, resulting in the formation of bismuth stibate (Bi_3SbO_7) as a binary impurity phase. Oxide precursors, including bismuth(III) and antimony(III,V) oxides, are fixed in the samples up to 750 °C, at which point the intermediate cubic phase $Bi_3M_{2/3}Sb_{7/3}O_{11}$ (sp. gr. *Pn-3*, *M = Zn*, *Ni*) is formed in the zinc system. Interacting with transition element oxides, it is transformed into pyrochlore. An intermediate phase with the $Bi_{4.66}Ca_{1.09}VO_{10.5}$ structure (sp. gr. *Pnnm*) was found in the magnesium system. The unit cell parameter of pyrochlore for two samples has a minimum value at 800 °C, which is associated with the onset of high-temperature synthesis of pyrochlore. The synthesis of phase-pure pyrochlores is confirmed by high-resolution Raman spectroscopy. The data interpretation showed that the cations in Ni/Zn pyrochlore are more likely to be incorporated into bismuth positions than in Ni/Mg pyrochlore. The nickel–magnesium pyrochlore is characterized by a low-porosity microstructure, with grain sizes of up to 3 μm, according to SEM data. Zinc oxide has a sintering effect on ceramics. Therefore, the grain size in ceramics is large and varies from 2 to 7 μm.

Keywords: pyrochlore; bismuth stibate; transition 3d-elements; Raman spectroscopy; phase formation

check for updates

Academic Editor: Narcis Avarvari

Received: 25 April 2025
Revised: 20 June 2025
Accepted: 27 June 2025
Published: 30 June 2025

Citation: Zhuk, N.A.; Nekipelov, S.V.; Petrova, O.V.; Makeev, B.A.; Isaenko, S.I.; Krzhizhanovskaya, M.G.; Parshukova, K.N.; Korolev, R.I.; Simpeleva, R.A. Synthesis, Phase Formation, and Raman Spectroscopy of Ni and Zn(Mg) Codoped Bismuth Stibate Pyrochlore. *Chemistry* **2025**, *7*, 110. https://doi.org/10.3390/chemistry7040110

Copyright: © 2025 by the authors. Licensee MDPI, Basel, Switzerland. This article is an open access article distributed under the terms and conditions of the Creative Commons Attribution (CC BY) license (https://creativecommons.org/licenses/by/4.0/).

1. Introduction

Bismuth-containing synthetic oxide pyrochlores attract the close attention of scientists due to their wide range of practically useful properties, including low synthesis temperatures and the capacity for significant variation in the chemical composition of ceramics.

This enables the study of the relationship between the composition structure and properties of bismuth-containing synthetic oxide pyrochlores [1–6]. Traditionally, complex bismuth-containing pyrochlores are classified as either semiconductors or dielectrics. The low dielectric losses and high permittivity of these materials, in conjunction with their adjustable temperature coefficient of capacitance, and their chemical inertness with respect to low-melting metal conductors, are significant factors in their consideration as promising materials for the manufacture of multilayer ceramic capacitors, resistors, thermistors, and tunable microwave dielectric components [6–10]. Bismuth-containing pyrochlores are also notable for their catalytic properties in the UV and visible ranges of the electromagnetic spectrum with respect to organic pollutants and they are a promising element of solar batteries [11–14]. The microstructure of ceramics has a significant influence on their physicochemical properties. In order to obtain ceramics of a uniform composition and controlled grain size, wet chemistry methods are most often used. Such methods include the sol–gel synthesis method and the hydrothermal method, as well as the method of coprecipitation with subsequent calcination [15–20]. The solid-phase synthesis method is characterized by the simplicity of its implementation, reduced labor intensity, and frequent independence from the sample preparation of the initial precursors and additional reagents. However, the process is associated with several disadvantages, including the necessity for careful primary and intermediate homogenization of the precursor mixture and a high-temperature treatment, which, in general, results in the formation of dense and low-porosity ceramics, with an uncontrolled grain size. In this regard, ceramics with potential catalytic properties are traditionally synthesized using solution methods. Conversely, ceramics with excellent dielectric properties, for which high density and low porosity are important, are produced using solid-phase synthesis. In regard to the solid-phase high-temperature synthesis of oxide pyrochlores based on bismuth stibate, the samples exhibit a loose, porous structure, with a small grain size [19–24]. In consideration of the aforementioned factors, the present study investigates the phase formation process of bismuth stibate-based pyrochlores, with a focus on determining the heat treatment conditions that lead to the synthesis of single-phase and low-porosity ceramics. The phase formation process of oxide pyrochlores was previously studied using niobium and tantalum bismuth-containing pyrochlores [25–32]. In [26], the process of evolution of the pyrochlore phase during the composition of $Bi_2Mg(Zn)_{1-x}M_xTa_2O_{9.5-\Delta}$ (M = Cr, Fe) was analyzed within the temperature range of 650–1050 °C. The influence of magnesium/zinc oxides on the process of evolution of the pyrochlore phase was established. As demonstrated, magnesium oxide activates the reactivity of orthotantalate at a high temperature, while zinc oxide promotes the low-temperature synthesis of pyrochlore. The synthesis of the pyrochlore phase is common to all systems, occurring as a result of the high-temperature interaction of bismuth orthotantalate (α-$BiTaO_4$) with oxide precursors in the temperature range of 850–1050 °C. As indicated in [26], the following phases, namely Bi_3TaO_7, $Bi_{25}FeO_{40}$, $Bi_6Cr_2O_{15}$, and $Bi_{16}CrO_{27}$, including chromium(VI) compounds, were identified as intermediate phases. It was shown that ceramics with an increased zinc oxide content are characterized by a low-porosity dense microstructure. The presence of magnesium oxide promotes the formation of porous ceramics. In [27], it was shown that during the synthesis of pyrochlores with the composition $Bi_2Mg(Zn)_{1-x}Ni_xTa_2O_9$, magnesium oxide reacts at temperatures above 800 °C, while nickel oxide reacts at temperatures up to 750 °C. The calcination temperature did not significantly affect the microstructure of the samples, and an increase in the calcination duration led to the fusion of grains, with the formation of larger particles. In [31], the phase formation process of a niobium pyrochlore of the complex composition $Bi_2Cr_{1/6}Mn_{1/6}Fe_{1/6}Co_{1/6}Ni_{1/6}Cu_{1/6}Nb_2O_{9+\Delta}$ (space group Fd-3m:2, a = 10.4937(2) Å) was studied. It was found that the synthesis proceeds through a series of

successive stages, during which a transition from Bi-rich to Bi-depleted compounds occurs. The precursor of the pyrochlore phase is bismuth orthoniobate involving the orthorhombic modification (α-$BiNbO_4$). The pyrochlore phase is formed as a result of doping bismuth orthoniobate with ions of transition elements. In the course of the synthesis, the following complex oxides were identified as intermediate phases: $Bi_{14}CrO_{24}$, $Bi_{25}FeO_{40}$, $BiNbO_4$, and $Bi_5Nb_3O_{15}$. The interaction between the initial oxide precursors was revealed to take place at a temperature above 500 °C. It was demonstrated that varying the duration of the heat treatment at each stage of synthesis did not qualitatively change the phase composition of the sample, but affected the quantitative ratio of the phases. Phase-pure pyrochlore in terms of the specified composition was ultimately obtained at 1050 °C. The resulting ceramics are characterized by a low-porosity and dense microstructure, with blurred grain boundaries.

The solid-phase synthesis of phase-pure pyrochlores, based on bismuth stibate, has a number of features. As emphasized above, fine-grained ceramics are formed, and the stoichiometric composition of the oxide ceramics does not coincide with that of pyrochlores based on bismuth niobate/tantalate [18,33,34]. The solid-phase synthesis of antimony pyrochlores is traditionally carried out using the stoichiometric and moisture-resistant antimony(III) oxide, the step-by-step and long-term calcination of which is necessary for the oxidation of the antimony to Sb(V). In the present article, we report on the synthesis and the results from the study of the phase formation process during the solid-phase synthesis of the new pyrochlores $Bi_{2.7}M_{0.46}Ni_{0.70}Sb_2O_{10+\Delta}$ (M = Mg, Zn).

2. Experimental Part

For the solid-phase synthesis of the $Bi_{2.7}M_{0.46}Ni_{0.70}Sb_2O_{10+\Delta}$ (M = Zn, Mg) samples, stoichiometric amounts of bismuth (III), antimony (III), nickel (II), and zinc/magnesium (II) oxides of analytical grade were used. The phase formation process was studied using Raman spectroscopy, electron scanning microscopy, and X-ray phase analysis of the samples, which were successively calcined in air at temperatures from 500 to 1050 °C (increments of 50 °C) for 15 h, at each stage of heat treatment. After each calcination in air, the sample was thoroughly homogenized and pressed again into the form of disks to ensure tight contact between the ceramic grains. X-ray data were collected using a Shimadzu 6000 X-ray diffractometer (Tokyo, Japan) ($Cu_{K\alpha}$ radiation; 2θ = 10–80°; scan rate 2.0°/min). Phase analysis was conducted through the PDXL2 program (Rigaku, Tokyo, Japan), using the PDF-2 (2020) database. Studies of the surface morphology of the preparations, elemental mapping, and local quantitative elemental analysis were carried out using scanning electron microscopy and energy-dispersive X-ray spectroscopy (Tescan VEGA 3LMN scanning electron microscope (Tescan, Czech Republic), INCA Energy 450 energy-dispersive spectrometer (Tescan, Prague, Czech Republic)). The unit cell parameters of the pyrochlores were calculated using the CSD-4 software package () [35]. Studies of the samples using Raman spectroscopy were carried out via a Ramos M520 high-resolution Raman microscope (SOL instruments, Minsk, Belarus) in the range of 80–3500 cm^{-1}. The spectra were recorded using a 600 nm grating and a 532 nm solid-state laser, with a power of 0.6 mW and a 50× objective lens with a Nexcope NE910 microscope (Nexcope, Ningbo, China). The spectral and spatial resolutions were approximately 5 cm^{-1} and 2 μm, respectively. The spectra were recorded at room temperature. Recording times of up to 60 s were used for the ceramic and parent oxide samples, without any visible damage to their surfaces or changes in the shape of the spectra. The Raman spectra were recorded at different points for each sample.

3. Results and Discussion

The phase formation process of antimony pyrochlores was studied for two compositions of $Bi_{2.7}M_{0.46}Ni_{0.70}Sb_2O_{10+\Delta}$ (M = Zn, Mg), using vibrational (Raman) spectroscopy, scanning electron microscopy, and X-ray phase analysis. The compositions presented are new, first synthesized, phase-pure cubic pyrochlores. Magnesium- and zinc-containing pyrochlores were selected for the study in order to trace the effect of magnesium and zinc on the phase formation process and the microstructure of ceramics, as well as the reproducibility of the experimental results. X-ray phase analysis was performed on the samples that were successively calcined in a temperature range of 500–1050 °C (with an increment of 50 °C) for 15 h, at each stage of the heat treatment. The stoichiometric formula of the samples was determined experimentally, as a result of a targeted search for the chemical composition of the samples, crystallizing into the structural type of pyrochlore without impurities. The variation in the molar ratio of Bi/Sb, Ni/Zn enabled the establishment of the optimal composition of Ni/Zn pyrochlores, which corresponds to the formula $Bi_{2.7}(Ni/Zn)_{1.16–1.22}Sb_2O_{10+\Delta}$. The stoichiometric formula of phase-pure pyrochlore $Bi_{2.7}M_{0.46}Ni_{0.70}Sb_2O_{10+\Delta}$ (M = Zn, Mg) differs significantly from the stoichiometric composition of previously synthesized pyrochlores based on bismuth niobate/tantalate $Bi_{2.7}M_{0.46}Ni_{0.70}Sb_2O_{10+\Delta}$ (M = Zn, Mg) [34], which may be associated with the smaller cationic radius of Sb(V) compared to the radii of Nb(V)/Ta(V) ($R_{c.n.-6}$(Nb(V)) = 0.64 Å; $R_{c.n.-6}$(Ta(V)) = 0.64 Å; $R_{c.n.-6}$(Sb(V)) = 0.60 Å) [36]. The X-ray diffraction patterns of the calcined $Bi_{2.7}Zn_{0.46}Ni_{0.70}Sb_2O_{10+\Delta}$ sample, measured at different temperatures, ranging from 500 to 1050 °C, are shown in Figure 1.

The presented X-ray diffraction patterns demonstrate that the phase composition of the sample is significantly dependent on the calcination temperature. The results of the phase composition studies on the sample, using electron microscopy and X-ray phase analysis, are presented in Table 1.

Table 1. Phase composition of the $Bi_{2.7}Zn_{0.46}Ni_{0.70}Sb_2O_{10+\Delta}$ sample calcined at 500–1050 °C, according to X-ray diffraction and elemental mapping data.

Synthesis Temperature, °C	Phase Composition of the Sample
1050	pyrochlore
950	pyrochlore
900	$Bi_3M_{2/3}Sb_{7/3}O_{11}$ (traces), pyrochlore
850	$Bi_3M_{2/3}Sb_{7/3}O_{11}$, pyrochlore
800	$Bi_3M_{2/3}Sb_{7/3}O_{11}$, pyrochlore, NiO (traces)
750	$Bi_3M_{2/3}Sb_{7/3}O_{11}$, pyrochlore, NiO, ZnO (traces)
700	Bi_2O_3, Sb_2O_4, Bi_3SbO_7 (traces), pyrochlore, NiO, ZnO
650	Bi_2O_3, Sb_2O_4, Bi_3SbO_7, pyrochlore, NiO, ZnO
600	Bi_2O_3, Sb_2O_4, Bi_3SbO_7, NiO, ZnO
550	Bi_2O_3, Sb_2O_4, Bi_3SbO_7, NiO, ZnO
500	Bi_2O_3, Sb_2O_4, Bi_3SbO_7, NiO, ZnO

As shown by the X-ray phase analysis (Figure S1), upon the low-temperature calcination of the sample (500–600 °C), the precursor phases are identified using the X-ray diffraction patterns: monoclinic phase α-Bi_2O_3 (sp. group $P2_1/c$) and cubic NiO (sp. group Fm-3m, No. 00-047-1049), hexagonal ZnO (sp. group P63mc), mixed antimony oxide Sb_2O_4 = $Sb(SbO_4)$ ($Pna2_1$, No. 01-078-2066), and the products of their interaction with bismuth oxide, Bi_3SbO_7 (sp. group Cmmm) [37–41]. As antimony(III) is oxidized, the amount of Bi_3SbO_7 increases and that of Bi_2O_3 ($P2_1/c$) decreases. With an increasing synthesis temperature (650–700 °C), a reaction between tribismuth stibate, antimony oxide Sb_2O_4, and the oxide of the transition 3d element (NiO, ZnO) becomes possible with the formation

of a pyrochlore phase (sp. gr. Fd-3m, No. 01-085-2835). In the international crystallographic database, ICSD, a cubic phase of the nickel pyrochlore $Bi_{1.76}Ni_{0.8}Sb_{1.37}O_7$ (sp. gr. Fd-3m, No. 227, card number 01-085-2835) was found [42], which most closely corresponds in regard to its chemical composition to the synthesized pyrochlore, $Bi_{2.7}Zn_{0.46}Ni_{0.70}Sb_2O_{10+\Delta}$ (1).

$$1.76Bi_3SbO_7 + 1.175Sb_2O_4 + 2.4MO + 0.79O_2 = 3Bi_{1.76}M_{0.8}Sb_{1.37}O_7 \text{ (M = Ni, Zn)} \quad (1)$$

The results of the X-ray diffraction studies and elemental mapping (Figure 2) do not enable the precise determination of the type of the transition element oxides that were involved in the reaction, since independent phases of nickel and zinc oxides are recorded in the samples up to a temperature of 800 °C (NiO) and 750 °C (ZnO). The high-temperature treatment of the sample (750–900 °C) led to the formation of a two-phase product, with a small amount of the initial nickel and zinc oxides. The cubic phase $Bi_3M_{2/3}Sb_{7/3}O_{11}$ (M-Ni, Zn) belonging to the $KSbO_3$ structural type (space group P*n*-3) [43–46] appears as an impurity phase, the amount of which is at its maximum at 750 °C. In the temperature range of 800–900 °C, the interaction of the impurity phase $Bi_3M_{2/3}Sb_{7/3}O_{11}$ with zinc and nickel oxides apparently occurs, and phase-pure pyrochlore of a given composition is formed (2):

$$0.9Bi_3M_{2/3}Sb_{7/3}O_{11} + 0.557MO = Bi_{2.7}M_{1.16}Sb_{2.0}O_{10+\Delta} \text{ (M = Ni, Zn)} \quad (2)$$

It is interesting to note that the formation and stability of the cubic phase $Bi_3M_{2/3}Sb_{7/3}O_{11}$ (M = Ni, Zn) are associated with the temperature range in terms of the existence of the cubic metastable phase, δ-Bi_2O_3 (sp. gr. *Pn-3m*), into which α-Bi_2O_3 (sp. gr. $P2_1/c$) transforms, near 729 °C [37]. It can be assumed that the synthesis of the cubic phase from oxide precursors is initiated by the phase transformation of α-Bi_2O_3 into a more active cubic δ-phase. In addition, it was shown that the synthesis of $Bi_3M_{2/3}Sb_{7/3}O_{11}$ (M = Ni, Zn) occurs from the oxides Bi_2O_3, NiO, MgO, and Sb_2O_4, which are present in sufficient quantities in the reaction mixture. This is evidenced by the phase composition of the sample calcined at 750 °C, which does not contain bismuth (III) and antimony (III, V) oxides. At a temperature of 900 °C, low-intensity reflections of the cubic phase $Bi_3M_{2/3}Sb_{7/3}O_{11}$ appear in the X-ray diffraction patterns; a single-phase sample, according to the X-ray diffraction data, was formed at a temperature of 900 °C; at 950 °C, a well-crystallized sample is formed, as evidenced by a decrease in the width of the diffraction lines.

Figure 2 shows the results of the elemental mapping of the $Bi_{2.7}Ni_{0.7}Zn_{0.46}Sb_2O_{10+\Delta}$ samples that were calcined at 950 °C. The experimental results show that a uniform distribution of transition elements is observed across the surface of the samples when synthesizing the sample at 850 °C and above. The non-monotonic nature of the change in the unit cell parameter of pyrochlore with an increasing calcination temperature in the sample is shown in Figure 3. As shown in Figure 3, the unit cell parameter of the pyrochlore phase has a maximum of 10.4737 Å in the sample calcined at 650 °C. During the high-temperature calcination of the sample, the unit cell parameter of pyrochlore decreases to 10.464 Å (at 800 °C) and then increases again to 10.474 Å. It can be assumed that the non-linear change in the cell constant is associated with the stages of pyrochlore phase formation. In the low-temperature range and at 650 °C, a non-stoichiometric pyrochlore phase is formed, which is evidenced by the presence of unreacted oxide precursors in the sample. As the calcination temperature increases, the unit cell parameter decreases to 800 °C and reaches a value of 10.464 Å, then begins to increase. The presence of a minimum in terms of the cell parameter upon heating was previously manifested during the phase formation of tantalum pyrochlores [26,27] and can be associated with the achievement of an equilibrium state in the distribution of ions in the crystallographic positions of pyrochlore. In this case, the pyrochlore formed at 650 °C can be considered as a nonequilibrium state.

It is understood that such a state is a metastable stressed state of the pyrochlore crystal structure, caused by the uneven distribution of ions in crystallographic positions, vacancies, defects, and geometric distortion of the polyhedral environment of the cations. As the temperature of the reaction mixture increases, thermal activation of the transition element oxides occurs, oxide precursors interact with early pyrochlore, and a stoichiometric cubic phase is formed. This stage of pyrochlore synthesis is accompanied by an increase in the unit cell parameter (over 800 °C). As the XRD shows, at a temperature of 850 °C, there is a noticeable decrease in the amount of impurity phases in the sample and an increase in the proportion of pyrochlore. Within the temperature range of 950–1050 °C, the cell constant changes insignificantly from 10.4722 to 10.474 Å, which indicates the completion of the pyrochlore phase formation process and its thermal stability within this temperature range.

Microphotographs of the synthesized preparations are shown in Figure 4. The samples synthesized at a temperature of 500–800 °C are characterized by a non-uniform microstructure, formed by heterogeneous grains, which is explained by the multiphase composition of the samples. At 850–900 °C, fine-grained porous ceramics are formed, the longitudinal grain size of which varies from 0.2 to 1 μm. Occasionally, faceted large grains of up to 2 μm in size appear. At a temperature of 950 °C, the porosity of the ceramics decreases, grain fusion is observed, with the formation of chaotically oriented, large, faceted grains, which are 2–7 μm in size. The local chemical analysis using energy dispersive spectroscopy showed that the chemical composition of the sample corresponds to the specified theoretical one. Thus, the high-temperature calcination of the sample at 950 °C for 15 h leads to the sintering of fine-grained ceramics and the creation of a low-porosity microstructure, without a loss of the stoichiometry of the pyrochlore composition.

The phase formation study of the magnesium pyrochlores was carried out on a sample with a composition similar to that of the zinc pyrochlores, namely $Bi_{2.7}Mg_{0.46}Ni_{0.70}Sb_2O_{10+\Delta}$. The X-ray diffraction patterns of the sample calcined at 550–1050 °C are shown in Figure 5.

The phase composition of the sample calcined at 500, 550 °C is practically no different from that of the zinc preparation, confirming the hypothesis that the interaction between the oxide precursors is inactive in the low-temperature range. As a result of the low-temperature calcination of the sample (500–600 °C), the X-ray diffraction patterns show reflections of the monoclinic phase α-Bi_2O_3 (sp. gr. $P2_1/c$), oxides NiO, MgO (sp. gr. Fm-3m, No. 00-047-1049), mixed antimony oxide $Sb_2O_4 = Sb(SbO_4)$ ($Pna2_1$, No. 01-078-2066), and the products of their interaction, Bi_3SbO_7. At 600 °C, the interaction between antimony and bismuth oxides is activated and the X-ray diffraction pattern identifies the reflections of Bi_3SbO_7, which is present in the sample, recording the largest amount, compared to the zinc preparation. In addition to the monoclinic phase of α-Bi_2O_3, reflections of δ-Bi_2O_3 (sp. gr. Fm-3m, No. 01-076-2478) are recorded (Figure S2). In general, the phase composition of the magnesium and zinc preparations calcined at 650 °C is similar. Conversely, at 650 °C, in contrast to the zinc preparation, the proportion of the pyrochlore phase in the sample is higher, and a decrease in the intensity of the reflections of bismuth stibates, bismuth oxide, and nickel is observed. As the temperature increased to 700 °C, there was a decrease in the amount of impurity phases in the sample. However, the phase composition of the zinc and magnesium preparations is almost identical. As shown in Figure 1, Figure 4, Figures S1 and S2, the amount of impurities in the magnesium pyrochlore is notably lower than in the zinc preparation. It is important to note that in regard to the diffraction pattern of the sample calcined at 700 and 750 °C, there is a second variant in terms of identifying the reflections in the diffraction pattern (Figure S2). According to this variant, an unknown phase for this system is formed, with a structure characteristic of orthorhombic $Bi_{4.66}Ca_{1.09}VO_{10.5}$ (sp. gr. *Pnnm*) [47]. For the zinc preparation at a temperature of 700 °C, a set of reflections characteristic of this phase also appears, which

indicates the reproducibility of the synthesis of the unknown compound and its low thermal stability. When the temperature is increased to 750 °C, reflections of the $Bi_3M_{2/3}Sb_{7/3}O_{11}$ impurity phase are identified in the zinc preparation. This phase is not formed in the magnesium preparation, whose phase composition is identical to the composition of the sample calcined at 700 °C. The X-ray diffraction pattern of the sample calcined at 800 °C shows low-intensity reflections of the $Bi_3M_{2/3}Sb_{7/3}O_{11}$ cubic phase, which is present in the sample in trace amounts at 850–950 °C. The elevated temperature and diminished quantity of the cubic phase may be attributable to the disparate chemical compositions of the cubic phases of $Bi_3M_{2/3}Sb_{7/3}O_{11}$ in both samples, resulting in divergent synthesis conditions and thermal stability. Additionally, the Mg system exhibits greater activity during the synthesis of the pyrochlore phase relative to the Zn system. The second reason is that in the magnesium system, the synthesis of the pyrochlore phase is more active compared to the zinc system. It is possible that there was an insufficiency of building material for the cubic phase, since all the transition element oxide, which may be nickel oxide, was spent on the synthesis of pyrochlore. As the elemental mapping shows (Figure 6), magnesium and nickel oxides do not appear as independent phases at a temperature of 850 and 700 °C, respectively. Assuming that the synthesis of the cubic phase occurs within the range of 750–800 °C, it can be hypothesized that it is not the composition with nickel that is synthesized so slowly, but rather the one with magnesium $Bi_3Mg_{2/3}Sb_{7/3}O_{11}$. It should be noted that the cubic phase of this composition was first synthesized and described in [42–45]. The work states that long-term high-temperature calcination at 800 °C is necessary for the targeted solid-phase synthesis of the magnesium phase. The results of the studies on the phase composition of the sample using electron microscopy and X-ray phase analysis are presented in Table 2.

Table 2. Phase composition of the $Bi_{2.7}Mg_{0.46}Ni_{0.70}Sb_2O_{10+\Delta}$ sample calcined at 550–1050 °C.

Synthesis Temperature, °C	Synthesis Temperature, °C
1050	pyrochlore
950	$Bi_3Mg_{2/3}Sb_{7/3}O_{11}$, pyrochlore
900	$Bi_3Mg_{2/3}Sb_{7/3}O_{11}$, pyrochlore
850	$Bi_3Mg_{2/3}Sb_{7/3}O_{11}$, pyrochlore
800	$Bi_3Mg_{2/3}Sb_{7/3}O_{11}$, pyrochlore
750	Bi_2O_3, Sb_2O_4, Bi_3SbO_7, pyrochlore, MgO
700	Bi_2O_3, Sb_2O_4, Bi_3SbO_7, pyrochlore, NiO, MgO
650	Bi_2O_3, Sb_2O_4, Bi_3SbO_7, pyrochlore, NiO, MgO
600	Bi_2O_3, Sb_2O_4, Bi_3SbO_7, NiO, MgO
550	Bi_2O_3, Sb_2O_4, Bi_3SbO_7, NiO, MgO
500	Bi_2O_3, Sb_2O_4, Bi_3SbO_7, NiO, MgO

The phase formation process of pyrochlores, based on bismuth niobate and tantalate, was the subject of the studies in [25–32]. As shown in the works [25–28,30–32], the process of synthesis of niobates and tantalates is generally similar. Many authors emphasize the formation of an intermediate phase, namely bismuth orthotantalate/orthoniobate, which is a precursor of the pyrochlore phase. The high-temperature interaction of $BiTaO_4$($BiNbO_4$) with the oxides of transition elements leads to the synthesis of pyrochlore. The synthesis process is accompanied by a number of peculiarities. Bismuth-rich phases, such as $Bi_{25}FeO_{40}$, $Bi_6Cr_2O_{15}$ and$Bi_{16}CrO_{27}$, including the chromium (VI) cation-containing phase, $Bi_6Cr_2O_{15}$, and $Bi_{16}CrO_{27}$ [26,31,32,48], have been identified as intermediate phases. In [28], it was established that the $BiNbO_4$ impurity phase has a negative effect on pyrochlore ceramics, since it chemically interacts with low-melting silver. The phase formation of antimony pyrochlores differs significantly. The synthesis proceeds through the formation of the intermediate phase, $Bi_3M_{2/3}Sb_{7/3}O_{11}$, which, being saturated with transition elements,

is transformed into pyrochlore. It is interesting to note that the phase composition for bismuth and antimony formally corresponds to the pyrochlore formula, with a deficiency of the transition element M: $Bi_3M_{2/3}Sb_{7/3}O_{11} = Bi_{2.7}M_{0.6}Sb_{2.1}O_{9.9}$. Apparently, the special course of the synthesis of antimony pyrochlores is due to the possibility of the synthesis of this phase, which is not typical for compositions with niobium or tantalum.

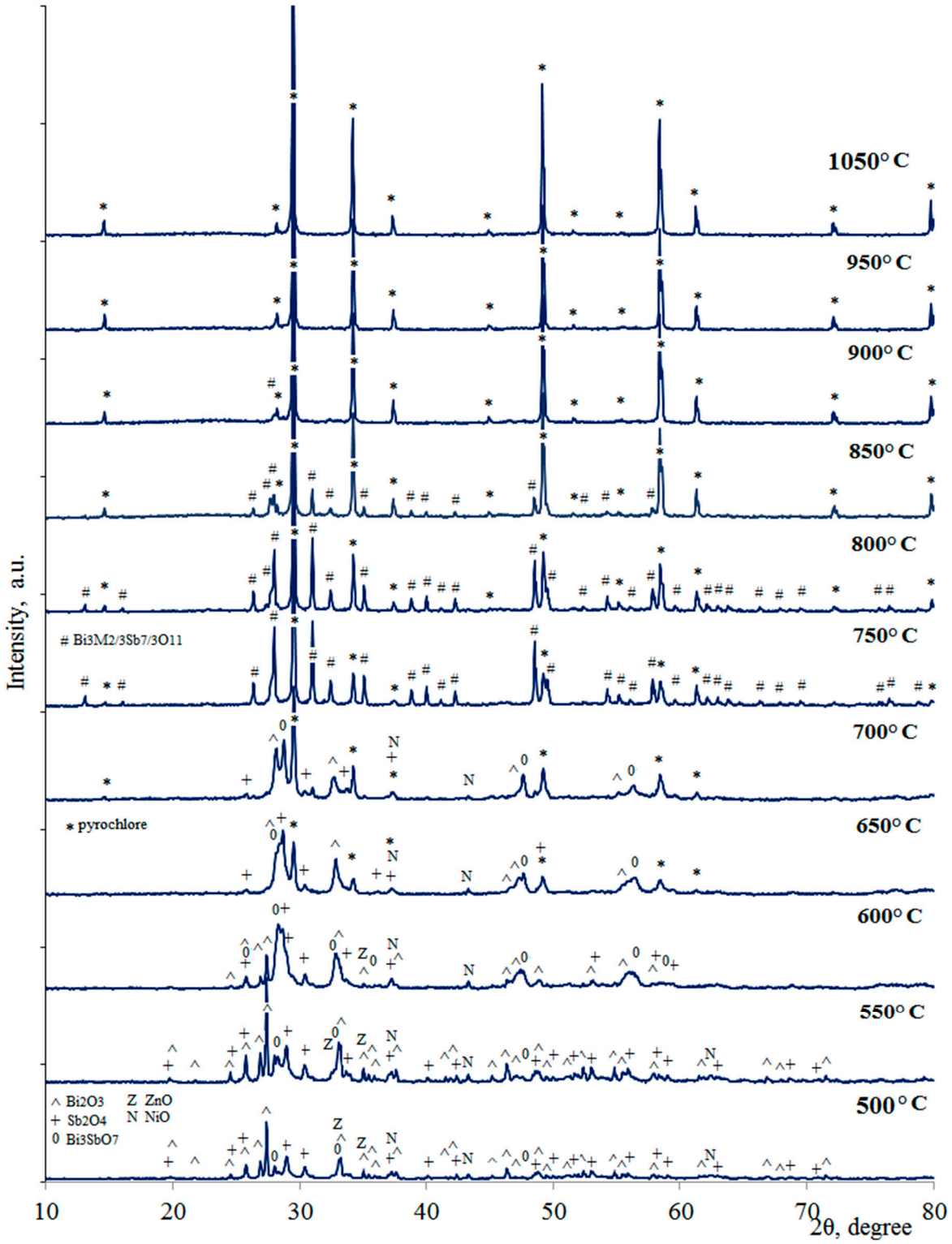


Figure 1. X-ray diffraction patterns of the $Bi_{2.7}Zn_{0.46}Ni_{0.70}Sb_2O_{10+\Delta}$ sample synthesized at temperatures, from 500 to 1050 °C.

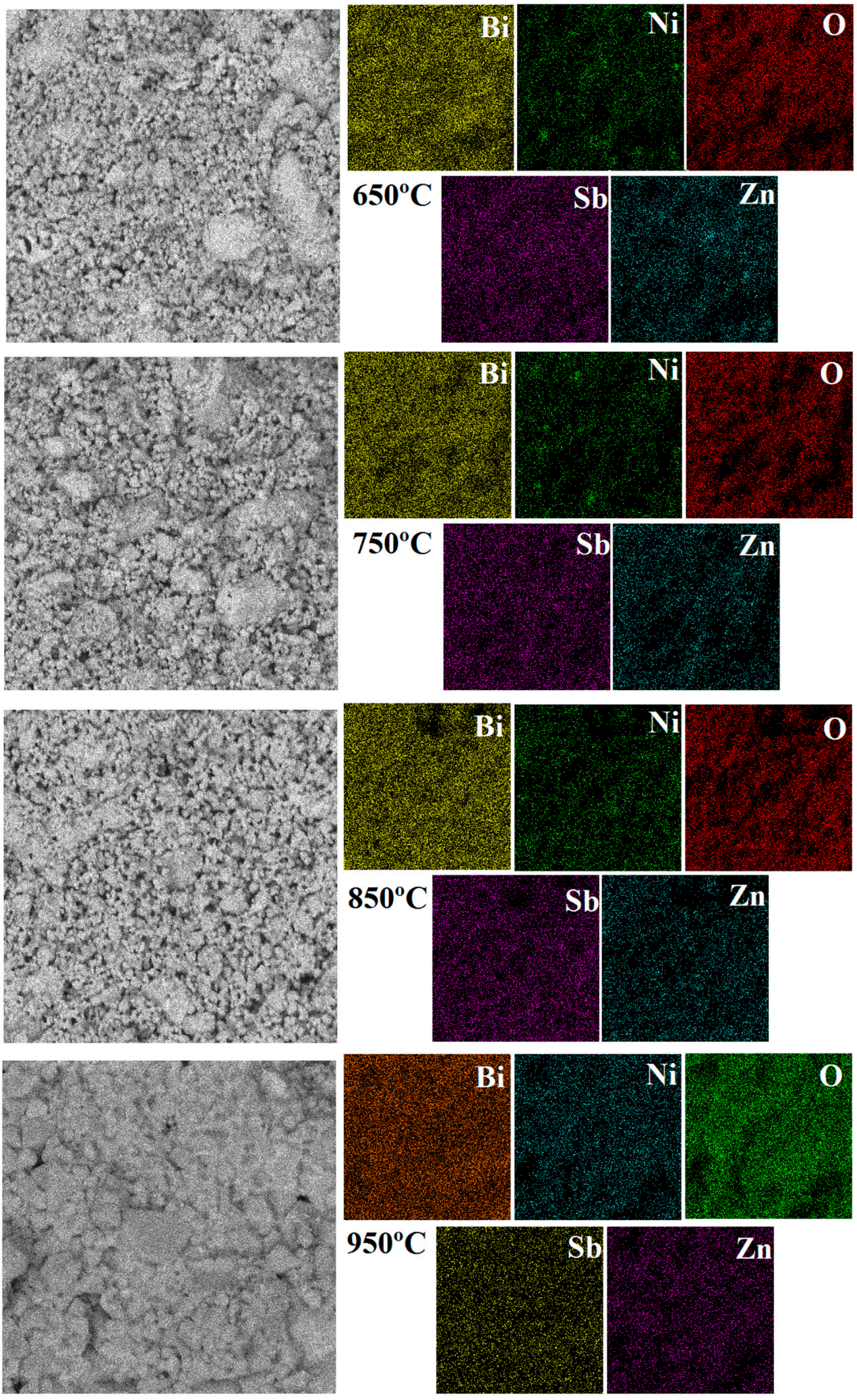


Figure 2. EDS mapping of the $Bi_{2.7}Zn_{0.46}Ni_{0.70}Sb_2O_{10+\Delta}$ sample synthesized at temperatures from 650 to 950 °C.

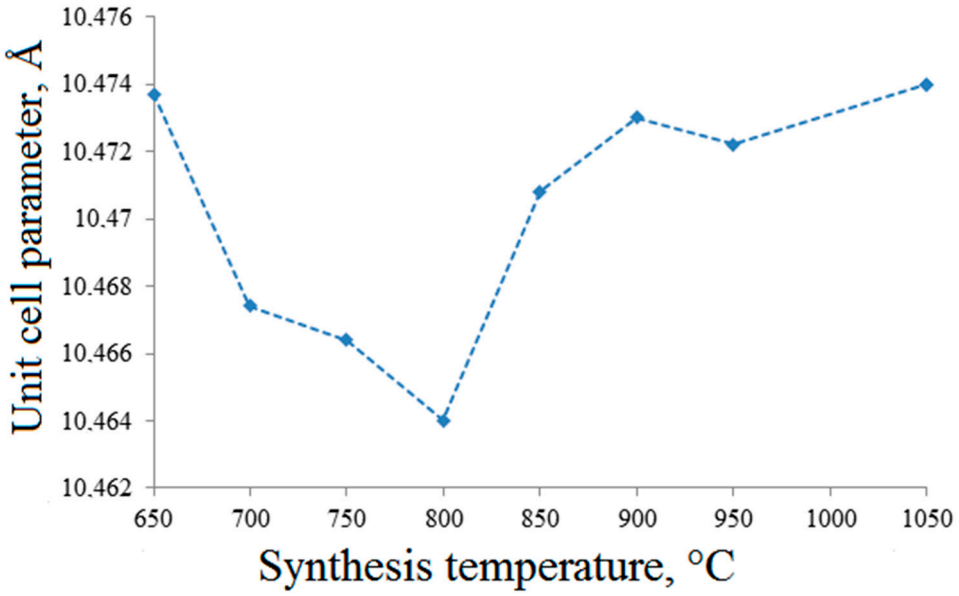


Figure 3. Change in the unit cell parameter of the pyrochlore phase in the $Bi_{2.7}Zn_{0.46}Ni_{0.70}Sb_2O_{10+\Delta}$ sample, depending on the synthesis temperature.

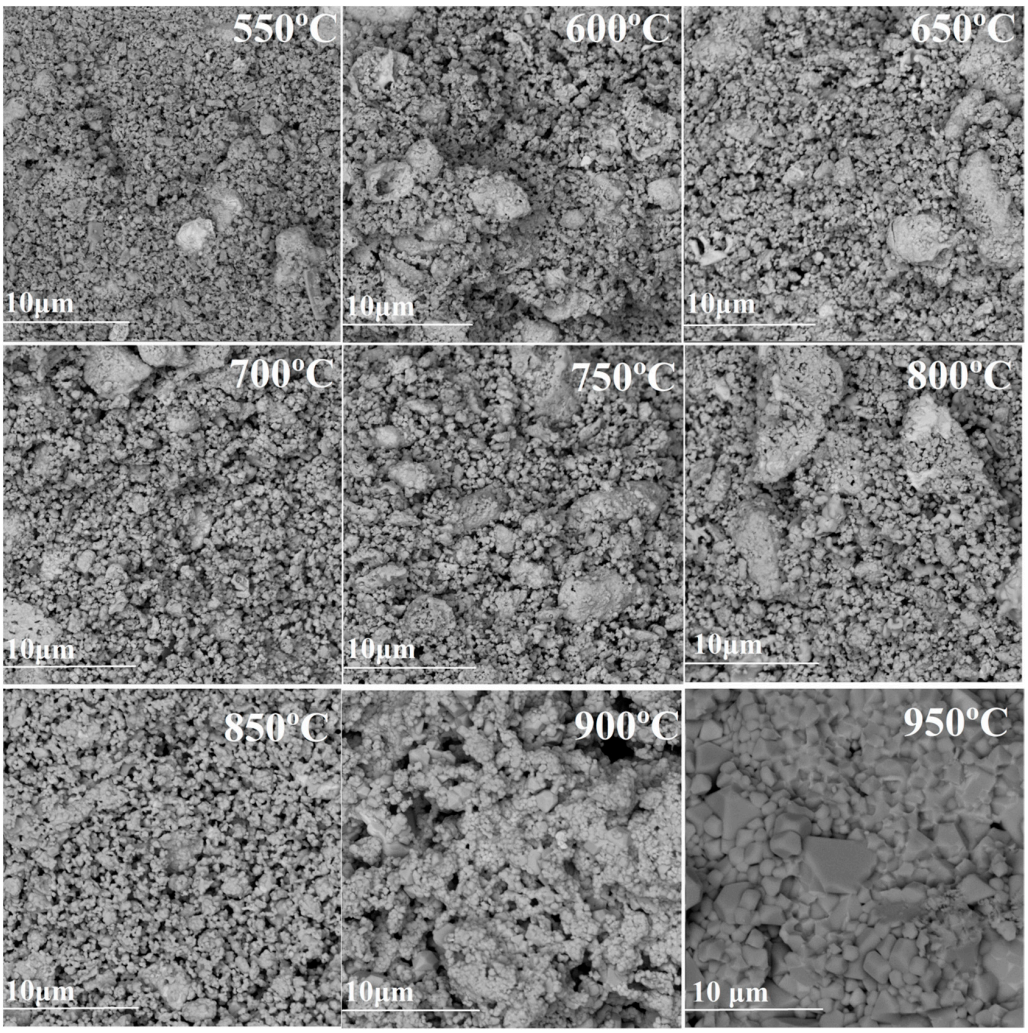


Figure 4. Micrographs of the surface of the $Bi_{2.7}Zn_{0.46}Ni_{0.70}Sb_2O_{10+\Delta}$ samples, synthesized at temperatures from 650 and 1050 °C.

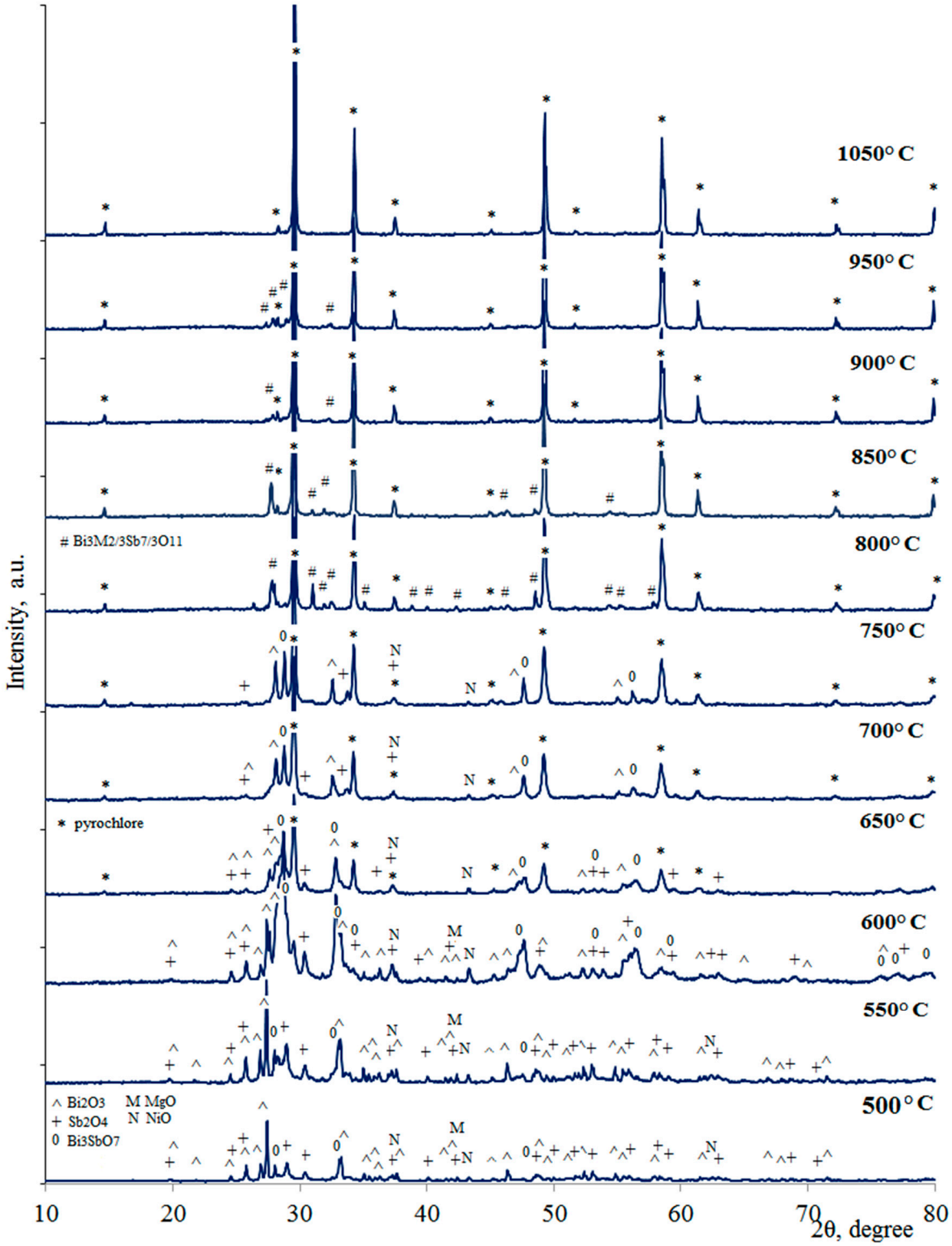


Figure 5. X-ray powder diffraction patterns of the $Bi_{2.7}Mg_{0.46}Ni_{0.70}Sb_2O_{10+\Delta}$ sample calcined at 550–1050 °C.

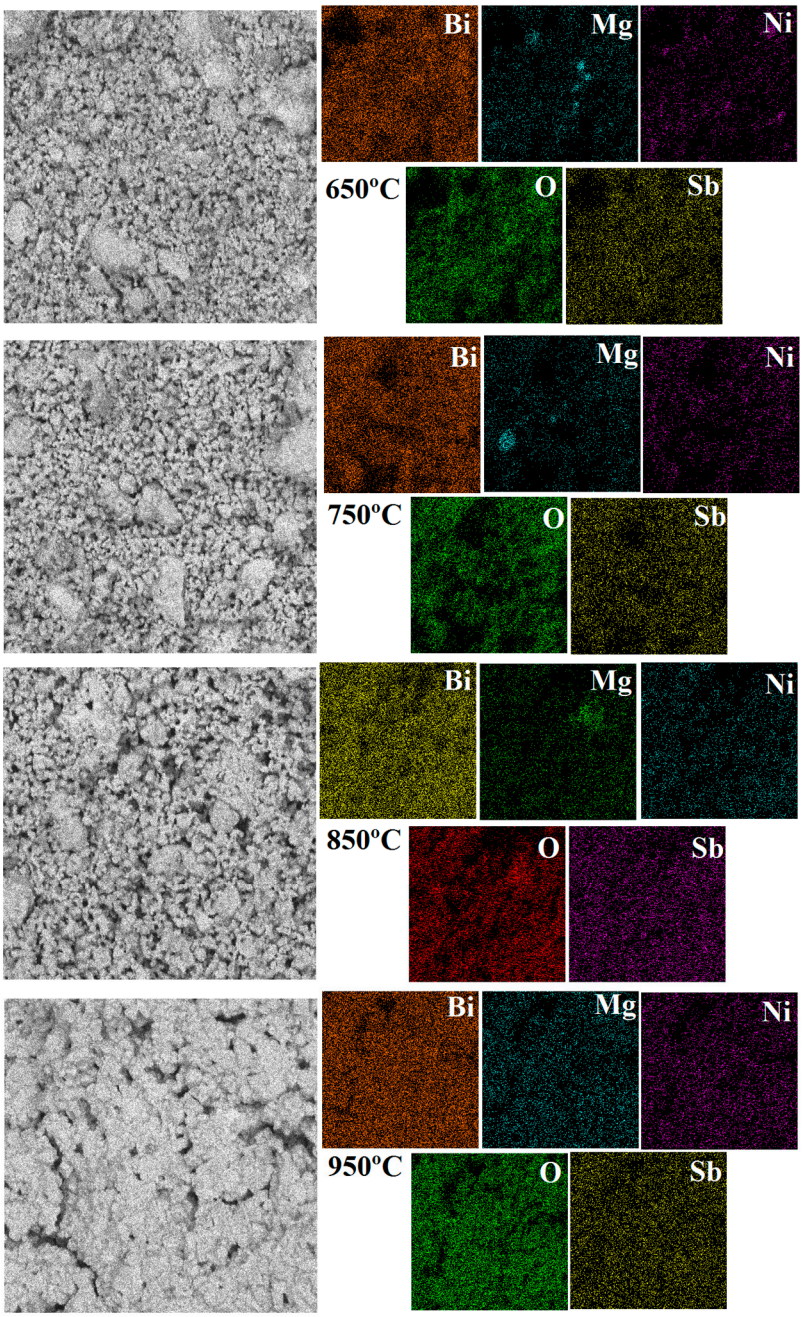


Figure 6. EDS mapping of the $Bi_{2.7}Mg_{0.46}Ni_{0.70}Sb_2O_{10+\Delta}$ sample synthesized at temperatures from 650 to 950 °C.

The distinguishing characteristic of antimony pyrochlores, in contrast to tantalum/niobium pyrochlores, is the formation of nanocrystalline ceramics, even through solid-phase synthesis.

Microphotographs of the synthesized magnesium preparations are shown in Figure 7. The samples synthesized at a temperature of 550–750 °C are characterized by a non-uniform microstructure, containing grains of different shapes and chemical compositions, resulting from the multiphase composition of the samples. The characteristic fine-grained microstructure of antimony pyrochlore is formed at a temperature of 800–850 °C. According to the SEM data, the samples are characterized by a porous microstructure formed by unbound ceramic grains of an elongated shape and with a longitudinal size of 0.5–2.0 μm. Increases in temperature to 950 °C results in grain growth, observed in regard to the formation of larger grains, with a size of 2–3 μm. It is interesting to note that magnesium pyrochlores

and zinc antimony pyrochlores differ in regard to their microstructure. Zinc pyrochlores are characterized by a dense, virtually pore-free microstructure, formed partially by organelles, with a grain size of 2–7 μm, while magnesium pyrochlores have a maximum grain size of 3 μm. Thus, the microstructure of ceramics can be regulated by high-temperature calcination, which causes grain growth, or by adding sintering additives, which include zinc oxide. The distinguishing characteristic of antimony pyrochlores, in contrast to tantalum/niobium pyrochlores, is the formation of nanocrystalline ceramics, even through solid-phase synthesis.

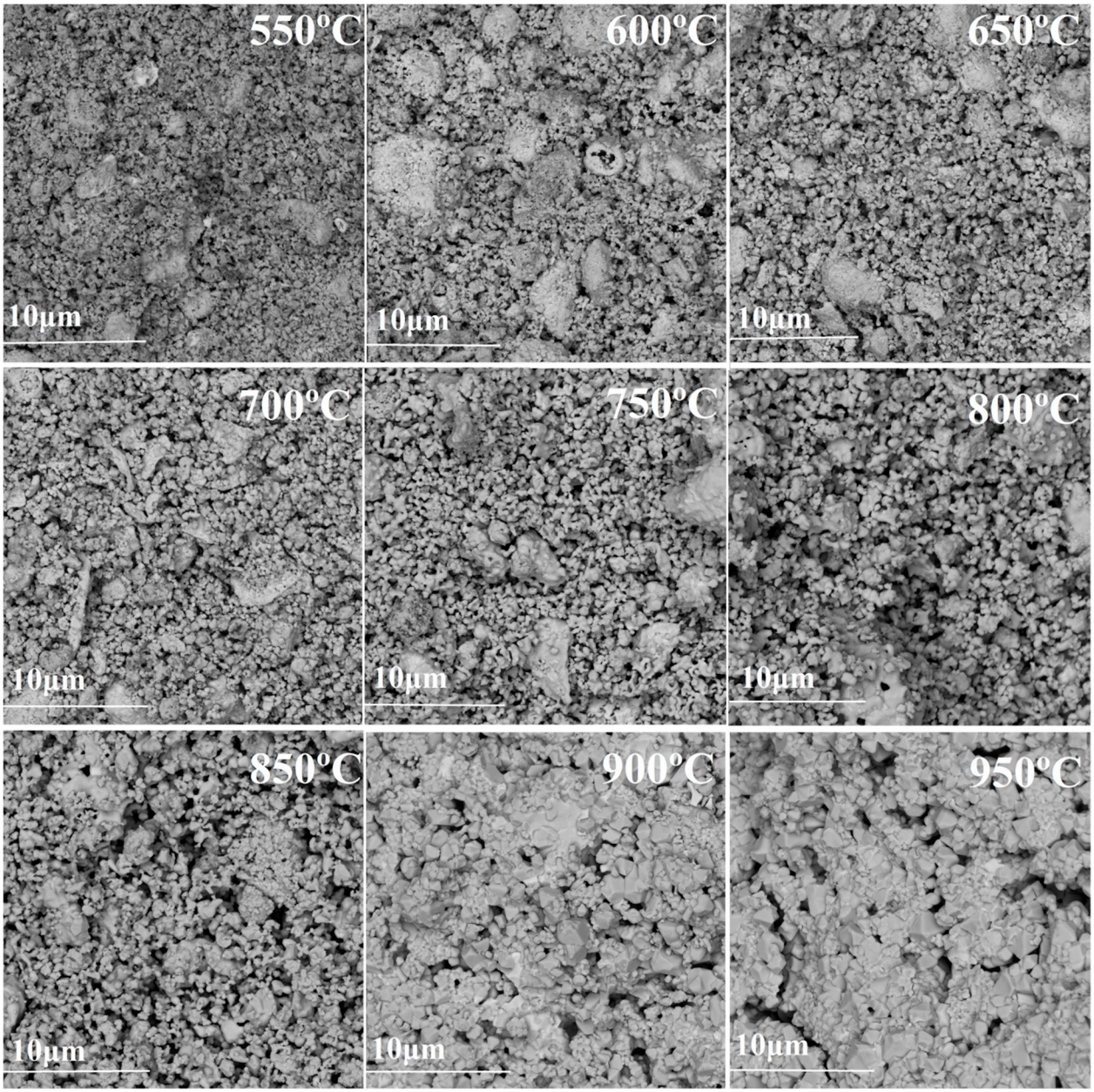


Figure 7. Microphotographs of the surface of the $Bi_{2.7}Mg_{0.46}Ni_{0.70}Sb_2O_{10+\Delta}$ samples synthesized at temperatures of 550–950 °C.

The non-monotonic nature of the change in the unit cell parameter of antimony pyrochlores with an increasing calcination temperature of the $Bi_{2.7}Ni_{0.7}Mg_{0.46}Sb_2O_{10+\Delta}$ samples is shown in Figure 8. As Figure 8 shows, the unit cell parameter of the pyrochlore phase has a minimum value at 10.4585 Å for the sample calcined at 800 °C, as observed in

the zinc preparations. It can be assumed that the non-linear change in the cell constant is associated with the stages of formation of the pyrochlore phase. In the low-temperature range and at 650 °C, a nonequilibrium non-stoichiometric cubic phase of pyrochlore is formed, as evidenced by the presence of unreacted oxide precursors in the sample. As the calcination temperature increases to 800 °C, the ions are redistributed in the pyrochlore structure, reaching an equilibrium state. As shown by the XRD patterns, at 850 °C, the active interaction of oxide precursors with pyrochlore and the formation of a stoichiometric cubic phase occurs. At the synthesis temperature of phase-pure pyrochlore in the range of 950–1050 °C, the cell constant changes insignificantly from 10.4655 to 10.4690 Å. The unit cell parameter of magnesium pyrochlores (10.4690 Å) is smaller than that of zinc pyrochlore (10.4740 Å), which may be due to the difference in the ionic radii of zinc and magnesium cations ($R(Mg(II)_{c.n.-6}$ = 0.72 Å), $R(Zn(II)_{c.n.-6}$ = 0.74 Å) [36]. In general, the unit cell parameters of the studied pyrochlores are comparable to the unit cell parameters of known bismuth-containing pyrochlores. In [42], the definition region of nickel-containing pyrochlores, based on bismuth stibate, is $(Bi_{2-x}Ni_x)Ni_{2/3-y}Sb_{4/3}$ + yO7-δ, $0.1 \leq x \leq 0.35$, $0 \leq y \leq 0.1$), whose unit cell parameter, depending on the stoichiometry of pyrochlores, varies in the range of 10.4690–10.4740 Å, and does not contradict our values. The cell constant of pyrochlore (a = 10.471 Å) of the composition Bi_2O_3:Fe_2O_3:Sb_2O_5 = 0.4500:0.3030:0.2407 practically corresponds to the cell parameters of the pyrochlores studied by us [19,43].

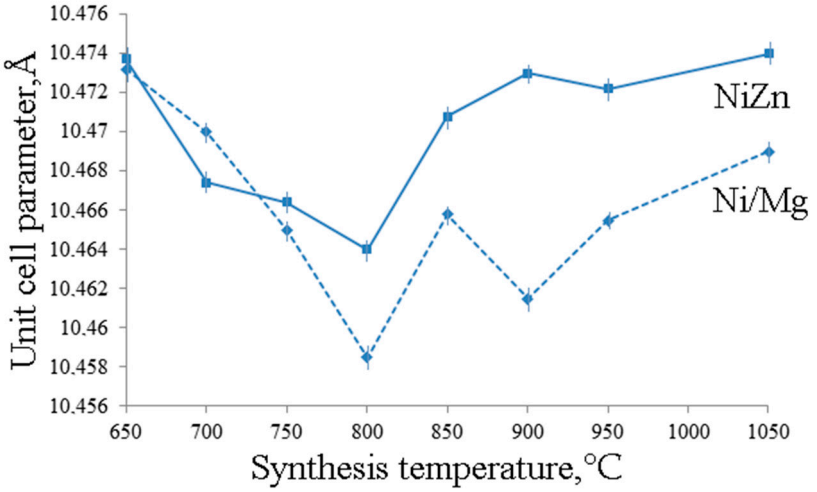


Figure 8. Change in the unit cell parameters of $Bi_{2.7}Mg_{0.46}Ni_{0.7}Sb_2O_{10+\Delta}$ and $Bi_{2.7}Zn_{0.46}Ni_{0.7}Sb_2O_{10+\Delta}$ depending on the synthesis temperature.

The formation of antimony pyrochlores was confirmed using Raman spectroscopy. Figure 9 shows the Raman spectra of $Bi_{2.7}Ni_{0.7}M_{0.46}Sb_2O_{10+\Delta}$ (M = Zn, Mg) at different sintering temperatures. As Figure 9 shows, the main details of the spectra are already formed at a temperature of 750 °C and remain virtually unchanged upon sintering at higher temperatures. This result correlates with the XRD data, which indicates that the pyrochlore phase is fixed in the samples calcined at 650 °C. At 750 °C, the samples contain impurity signals at 120 cm^{-1} and 205 cm^{-1} in the magnesium composition, and at 195 cm^{-1} and 200 cm^{-1} in the zinc composition, which is due to the presence of different impurity phases in the samples. The observed discrepancy between the vibrational modes for these samples indicates that the samples have different impurity compositions and different phase formation pathways. Indeed, at 750 °C, an unknown phase of the $Bi_{2.7}M_{0.46}$ $Ni_{0.7}Sb_2O_{10+\Delta}$ type is present in the magnesium composition, and a cubic phase of $Bi_3M_{2/3}Sb_{7/3}O_{11}$ is present in the zinc composition. At the maximum sintering temperature of the samples, of 850 °C, the

spectra of these samples are almost identical (Figure 9), which indicates that their crystal structure is formed in an identical way and there are no impurities in the samples. The appearance of the spectra themselves and their main peaks are generally characteristic of pyrochlores.

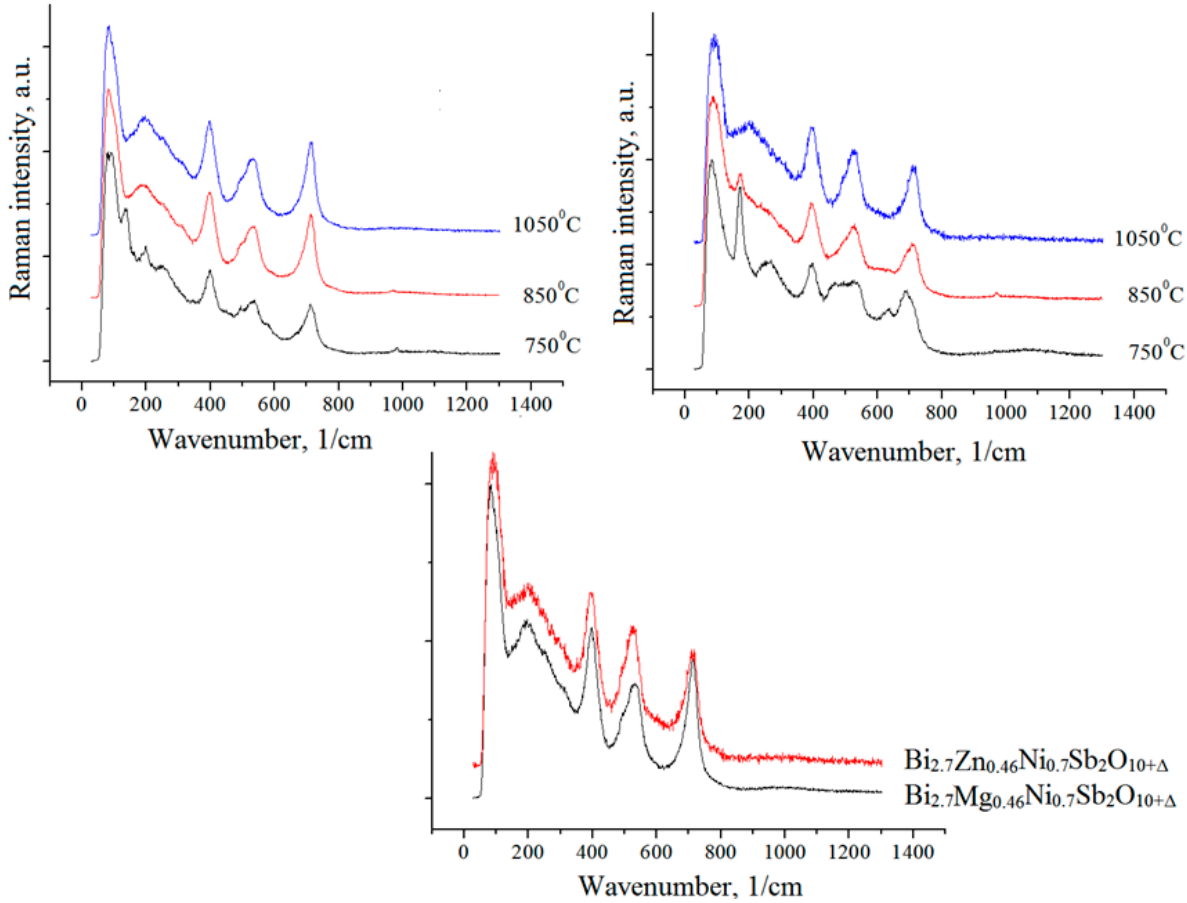


Figure 9. Raman spectra of $Bi_{2.7}M_{0.46}Ni_{0.7}Sb_2O_{10+\Delta}$ (M-Mg, Zn) ceramics synthesized at 750, 850, and 1050 °C.

As is known [2,3], the face-centered cubic structure of pyrochlores consists of two independent and interpenetrating sublattices, B_2O_6 and A_2O'. The cationic sublattice of B_2O_6 is formed by octahedra [BO_6] connected at the corner apex. The sublattice A_2O' has an anticristobalite structure, formed by tetrahedra [$O'A_4$]. The group-theoretical analysis for the ideal pyrochlore structure indicates the existence of 25 vibrational modes [49–52], as shown in the following equation.

$$\Gamma = A_{1g}(R) + E_g(R) + 4F_{2g}(R) + 7F_{1u}(IR) + 4F_{2u} + 2F_{1g} + 3A_{2u} + 3E_u \quad (3)$$

Among all the 25 optical modes, only 6 (A_{1g}, E_g, and $4F_{2g}$) are Raman active (R) and include only the vibrations of oxygen atoms. Vibrations of A and B cations and oxygen ions are observed in the IR spectrum. The structural disordering of the crystal lattices of bismuth-containing pyrochlores leads to a decrease in the positional symmetry of A and O′ atoms [52]. As a result of a decrease in the strictness of the selection rules, new bands can be observed in their Raman spectra, which appeared due to the splitting of optical modes, as well as bands active in the IR spectra. In addition, the variation in the size and mass of the transition metal in the A and B positions results in changes to the force constants for the A-O, A-O′, and B-O vibrational modes and leads to the observed

shifts of the bands in the Raman spectra [51]. An attempt was made to identify the spectra of $Bi_{2.7}Ni_{0.7}M_{0.46}Sb_2O_{10}$ (M = Zn, Mg) taking into account the data known from the literature, characteristic of bismuth-containing pyrochlores and those doped with metal atoms (Table 3). The identification of the vibrational modes and their symmetry was made on the basis of an analysis of the data in the literature [24,49–57]. As Figure 9 shows, in the Raman spectra of the studied pyrochlores, bands are observed in the ranges <200, 200–400, and 400–700 cm^{-1}. In the Raman spectra of pyrochlores with an ideal structure, the Raman bands lie in the region above 200 cm^{-1} [56]. In this regard, the bands below 200 cm^{-1} are attributed to F1u modes active in the IR spectra, the appearance of which is associated with disordering of the crystal lattice of pyrochlores [55,57]. As a rule, the vibrations of oxygen ions associated with heavy Bi cations (O′-Bi-O′, O-Bi-O′, and Bi-BO_6 vibrations) lie within this frequency range [53,55]. In the Raman spectra of the studied samples, an intense line appears near 80 cm^{-1} (Figures 9 and 10). It is interesting to note that the position of the maximum for the Zn/Mg pyrochlore samples is different (Figure 10a,b). It can be noted that for the zinc preparation, a shift in the maximum of the band to the long-wave region of 93 cm^{-1} is recorded. The observed discrepancy between the position of the F1u mode for both pyrochlores indicates a different distribution of the transition element cations, namely Mg, Ni, and Zn, in the bismuth position. Since the mass of bismuth cations is greater than the mass of zinc, nickel, and magnesium cations, and the shift is pronounced for zinc pyrochlore, it can be deduced that zinc or nickel cations occupy bismuth positions to a greater extent than magnesium/nickel. Zinc cations demonstrate a greater propensity for tetrahedral positions than nickel cations, thereby resulting in a partial distribution of zinc cations in the bismuth position. In the region of 200–400 cm^{-1}, in particular at 195–203 cm^{-1} and 397–400 cm^{-1}, vibrations are associated with the F_{2g} mode [56]. Vibrations in the range of 400–700 cm^{-1} are typically attributed to [BO_6] octahedra. In the Raman spectra of "ideal" pyrochlores, as a rule, two bands are observed, attributed to the A_{1g} and F_{2g} modes [55]. In the studied spectra from this range, several bands can be distinguished near 493, 527–539, and 710–714 sm^{-1} (Figures 9 and 10).

Table 3. Frequencies of vibrational modes in the Raman spectra of $Bi_{2.7}M_{0.46}Ni_{0.7}Sb_2O_{10+\Delta}$ (M = Zn, Ni).

Frequency (sm^{-1})		Symmetry	Identification
Ni/Mg	Ni/Zn		
Pyrochlore			
80	93	F_{1u}	Angular oscillations O-A-O, O-A-O′, O′-A-O′, chemical bond vibrations A-BO_6
195	203	$E_g + F_{2g}$	Chemical bond vibrations A-O
400	397	F_{2g}	Chemical bond vibrations *B*-O
493	493	A_{1g}	Bond O-*Sb*-O in the octahedron SbO_6
539	527	A_{1g}	Bond O-*M*-O in the octahedron MO_6 (M-Ni, Mg, Zn)
710	714	F_{2g}	Chemical bond vibrations *B*-O

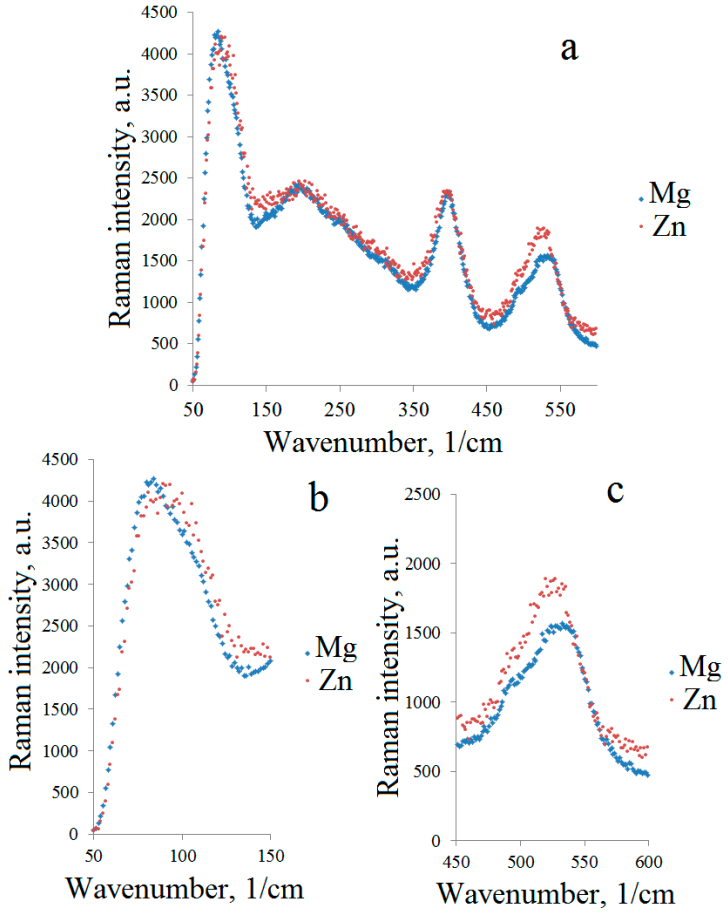


Figure 10. Comparison of Raman spectra of $Bi_{2.7}M_{0.46}Ni_{0.7}Sb_2O_{10+\Delta}$ (M = Mg, Zn) ceramics in the ranges 50–600 cm^{-1} (**a**); 50–150 cm^{-1} (**b**); and 450–600 cm^{-1} (**c**).

The broad composite band near 540 cm^{-1} is a superposition of two closely located bands at 493 and 527–539 cm^{-1}, with an intensity that differs by a factor of two. The intensity of the bands can correlate with the degree of polarization of the M/Sb-O, M = Mg, Ni, Zn bond in the octahedra. According to the literature [55,56], these bands are attributed to the A_{1g} vibrational modes of the corresponding octahedra. Since the band at 493 cm^{-1} did not change its position for both pyrochlores, it can be associated with vibrations of the Sb-O bond in the antimony octahedra [SbO_6]. The frequency of the most intense band at 527–539 cm^{-1} varies depending on the nature of the dopants. For the Mg/Ni pyrochlore, it is equal to 539 cm^{-1}, and, for the Zn/Ni pyrochlore, it is lower and equal to 527 cm^{-1}, which indicates vibrations of the [MO_6] octahedra (M = Ni, Mg, Zn). The most significant shift towards the long-wavelength region for the Mg/Ni pyrochlore correlates with the masses of the dopants, in particular Mg(II), which occupy the octahedral positions of antimony(V). The intense band at 710–714 cm^{-1}, observed in the Raman spectra of various bismuth pyrochlores, is attributed to the high-frequency F_{2g} vibration [56]. For both pyrochlores, the position of the band changes insignificantly.

The results of the studies showed that the main bands in the low-energy region are attributed to vibrations in the bismuth sublattice, and the high-energy ones are attributed to vibrations in the BO_6 octahedron structure. This phenomenon is explained by the fact that bismuth cations are significantly heavier than antimony cations and dopants. The observed differences in the Raman spectra for the two compositions may mean that zinc, magnesium, and nickel cations, in both samples, are introduced into crystallographic positions differently. Cations in the Ni/Zn pyrochlore are predominantly introduced into the bismuth positions, with the highest probability being zinc cations. The appearance of

composite bands in the region of octahedral vibrations indicates the distribution of dopants predominantly in octahedral positions.

The synthesized compounds may be promising as photocatalysts and high-frequency dielectrics. The manifestation of these properties is favored by the microstructure of the compounds, formed by grains in the nanometer range, and the low porosity of the ceramics. Our conclusions do not contradict literary sources [19,20], according to which antimony pyrochlores have outstanding catalytic properties in the visible and UV ranges with respect to pollutants of an organic and inorganic nature.

4. Conclusions

The solid-phase synthesis of $Bi_{2.7}M_{0.46}Ni_{0.70}Sb_2O_{10+\Delta}$ (M = Zn, Mg) pyrochlores is a complex multi-stage process. For each system, the phase formation process in the range of 500–1050 °C was analyzed, which occurs through the synthesis of poorly studied intermediate phases of the $Bi_3M_{2/3}Sb_{7/3}O_{11}$ (sp. gr. *Pn-3*) and $Bi_{4.66}Ca_{1.09}VO_{10.5}$ (sp. gr. *Pnnm*) types, which are not typical of tantalum and niobium systems. It was shown that oxide precursors, including bismuth(III) and antimony(III, V) oxides, interact inactively with each other and are fixed in the samples up to 750 °C. Single-phase pyrochlores are synthesized at 950–1050 °C. With an increasing calcination temperature, the microstructure of the ceramics becomes dense and low porosity and active grain growth is observed, especially in the case of zinc-containing samples. The formation of phase-pure ceramics in both cases is confirmed by studies using Raman spectroscopy. Raman spectroscopy indicated a partial distribution of transition element cations in the bismuth position for the Ni/Zn pyrochlore.

Supplementary Materials: The following supporting information can be downloaded at: https://www.mdpi.com/article/10.3390/chemistry7040110/s1, X-ray powder diffraction patterns of the $Bi_{2.7}Zn_{0.46}Ni_{0.70}Sb_2O_{10+\Delta}$ sample (synthesized at temperatures of 600, 650, 800, and 850 °C) and of the $Bi_{2.7}Mg_{0.46}Ni_{0.70}Sb_2O_{10+\Delta}$ sample (synthesized at temperatures of 600, 750, and 800 °C).

Author Contributions: Conceptualization, N.A.Z.; formal analysis, O.V.P.; investigation, N.A.Z., S.V.N., B.A.M., S.I.I., M.G.K., K.N.P., R.I.K. and R.A.S.; resources, M.G.K., S.V.N., B.A.M. and S.I.I.; validation, N.A.Z., S.V.N., B.A.M., S.I.I., M.G.K., K.N.P., R.I.K. and R.A.S.; visualization, N.A.Z., S.V.N. and M.G.K.; writing—original draft, N.A.Z. and S.V.N. All authors have read and agreed to the published version of the manuscript.

Funding: This research was funded by Saint-Petersburg State University research project 125021702335-5.

Data Availability Statement: The original contributions presented in the study are included in the article/Supplementary Materials. Further inquiries can be directed to the corresponding author.

Conflicts of Interest: The authors declare no conflict of interest.

References

1. Giampaoli, G.; Siritanon, T.; Day, B.; Li, J.; Subramanian, M.A. Temperature in-dependent low loss dielectrics based on quaternary pyrochlore oxides. *Prog. Solid. State Chem.* **2018**, *50*, 16–23. [CrossRef]
2. Subramanian, M.A.; Aravamudan, G.; Subba Rao, G.V. Oxide pyrochlores—A review. *Prog. Solid. State Chem.* **1983**, *15*, 55–143. [CrossRef]
3. McCauley, R.A. Structural Characteristics of Pyrochlore Formation. *J. Appl. Phys.* **1980**, *51*, 290–294. [CrossRef]
4. Vanderah, T.A.; Lufaso, M.W.; Adler, A.U.; Levin, I.; Nino, J.C.; Provenzano, V.; Schenck, P.K. Subsolidus phase equilibria and properties in the system Bi_2O_3:$Mn_2O_3 \pm x$:Nb_2O_5. *J. Solid State Chem.* **2006**, *179*, 3467–3477. [CrossRef]
5. Vanderah, T.A.; Siegrist, T.; Lufaso, M.W.; Yeager, M.C.; Roth, R.S.; Nino, J.C.; Yates, S. Phase Formation and Properties in the System Bi_2O_3:$2CoO_{1+x}$:Nb_2O_5. *Eur. J. Inorg. Chem.* **2006**, *2006*, 4908–4914. [CrossRef]
6. Lufaso, M.W.; Vanderah, T.A.; Pazos, I.M.; Levin, I.; Roth, R.S.; Nino, J.C.; Provenzano, V.; Schenck, P.K. Phase formation, crystal chemistry, and properties in the system Bi_2O_3–Fe_2O_3–Nb_2O_5. *J. Solid State Chem.* **2006**, *179*, 3900–3910. [CrossRef]

7. Du, H.; Wang, H.; Yao, X. Observations on structural evolution and dielectric properties of oxygen-deficient pyrochlores. *Ceram. Int.* **2004**, *30*, 1383–1387. [CrossRef]
8. Huiling, D.; Xi, Y. Structural trends and dielectric properties of Bi-based pyrochlores. *J. Mater. Sci. Mater. Electron.* **2004**, *15*, 613–616. [CrossRef]
9. Cann, D.P.; Randall, C.A.; Shrout, T.R. Investigation of the dielectric properties of bismuth pyrochlores. *Solid State Commun.* **1996**, *100*, 529–534. [CrossRef]
10. Khaw, C.C.; Tan, K.B.; Lee, C.K. High temperature dielectric properties of cubic bismuth zinc tantalate. *Ceram. Int.* **2009**, *35*, 1473–1480. [CrossRef]
11. Murugesan, S.; Huda, M.N.; Yan, Y.; Al-Jassim, M.M.; Subramanian, V. Band-Engineered Bismuth Titanate Pyrochlores for Visible Light Photocatalysis. *J. Phys. Chem. C* **2010**, *114*, 10598–10605. [CrossRef]
12. Valant, M.; Babu, G.S.; Vrcon, M.; Kolodiazhnyi, T.; Axelsson, A.-K. Pyrochlore range from Bi_2O_3–Fe_2O_3–TeO_3 system for LTCC and photocatalysis and the crystal structure of new $Bi_3(Fe_{0.56}Te_{0.44})_3O_{11}$. *J. Am. Ceram. Soc.* **2011**, *95*, 644–650. [CrossRef]
13. Lomakin, M.S.; Proskurina, O.V.; Sergeev, A.A.; Buryanenko, I.V.; Semenov, V.G.; Voznesenskiy, S.S.; Gusarov, V.V. Crystal structure and optical properties of the Bi–Fe–W–O pyrochlore phase synthesized via a hydrothermal method. *J. Alloys Compd.* **2022**, *889*, 161598. [CrossRef]
14. Pandey, J.; Shrivastava, V.; Nagarajan, R. Metastable $Bi_2Zr_2O_7$ with Pyrochlore-like Structure: Stabilization, Oxygen Ion Conductivity, and Catalytic Properties. *Inorg. Chem.* **2018**, *57*, 13667–13678. [CrossRef]
15. Lomakin, M.S.; Proskurina, O.V.; Danilovich, D.P.; Panchuk, V.V.; Semenov, V.G.; Gusarov, V.V. Hydrothermal synthesis, phase formation and crystal chemistry of the pyrochlore/Bi_2WO_6 and pyrochlore/α–Fe_2O_3 composites in the Bi_2O_3–Fe_2O_3–WO_3 system. *J. Solid State Chem.* **2020**, *282*, 121064. [CrossRef]
16. Perenlei, G.; Talbot, P.C.; Martens, W.N. Sol-gel synthesis and characterization of cubic bismuth zinc niobium oxide nanopowders. *J. Nanomater.* **2014**, *2014*, 695973. [CrossRef]
17. Kahoul, A.; Nkeng, P.; Hammouche, A.; Naamoune, F.; Poillerat, G. A Sol–Gel Route for the Synthesis of $Bi_2Ru_2O_7$ Pyrochlore Oxide for Oxygen Reaction in Alkaline Medium. *J. Solid State Chem.* **2001**, *161*, 379–384. [CrossRef]
18. Zhuk, N.A.; Badanina, K.A.; Korolev, R.I.; Krzhizhanovskaya, M.G.; Sekushin, N.A.; Belyy, V.A.; Makeev, B.A. Sol–gel derived $Bi_2NiNb_2O_9$ pyrochlore: Synthesis, characterization and dielectric properties. *Ceram. Int.* **2024**, *50*, 50397–50409. [CrossRef]
19. Egorysheva, A.V.; Gajtko, O.M.; Rudnev, P.O.; Ellert, O.G.; Ivanov, V.K. Synthesis of Bi–Fe–Sb–O pyrochlore nanoparticles with visible-light photocatalytic activity. *Eur. J. Inorg. Chem.* **2016**, *2016*, 2193–2199. [CrossRef]
20. Egorysheva, A.V.; Plukchi, K.R.; Golodukhina, S.V.; Liberman, E.Y.; Ellert, O.G. Hydrothermal synthesis of highly dispersed Bi–Ni–Sb–O pyrochlore for catalytic oxidation of carbon monoxide. *Mendeleev Commun.* **2023**, *33*, 608–610. [CrossRef]
21. Jusoh, F.A.; Tan, K.B.; Zainal, Z.; Chen, S.K.; Khaw, C.C.; Lee, O.J.; Balachandran, R.; Murthy, H.C.A. Novel pyrochlore-structured bismuth iron antimonates: Structural, impedance and electrochemical studies. *Results Phys.* **2021**, *27*, 104542. [CrossRef]
22. Miles, G.C.; West, A.R. Pyrochlore Phases in the System ZnO-Bi_2O_3-Sb_2O_5: I. Stoichiometries and Phase Equilibria. *J. Am. Ceram. Soc.* **2006**, *89*, 1042–1046. [CrossRef]
23. Whitaker, M.J.; Marco, J.F.; Berry, F.J.; Raith, C.; Blackburn, E.; Greaves, C. Structural and magnetic characterisation of the pyrochlores $Bi_{2-x}Fe_x(FeSb)O_7$, (x = 0.1, 0.2, 0.3), $Nd_{1.8}Fe_{0.2}(FeSb)O_7$ and $Pr_2(FeSb)O_7$. *J. Solid State Chem.* **2013**, *198*, 316–322. [CrossRef]
24. Rahman, R.A.U.; Ruth, D.E.J.; Ramaswamy, M. Emerging scenario on displacive cubic bismuth pyrochlores (Bi,M)$MNO_{7-\delta}$ (M = transition metal, N = Nb, Ta, Sb) in context of their fascinating structural, dielectric and magnetic properties. *Ceram. Int.* **2020**, *46*, 14346–14360. [CrossRef]
25. Muraviov, V.A.; Makeev, B.A.; Krzhizhanovskaya, M.G.; Korolev, R.I.; Zhuk, N.A. Synthesis of $Bi_2NiTa_2O_9$ with a pyrochlore-type structure. *Glass Ceram.* **2022**, *95*, 40–46. [CrossRef]
26. Zhuk, N.A.; Makeev, B.A.; Krzhizhanovskaya, M.G.; Korolev, R.I. Effect of magnesium and zinc on phase formation of pyrochlore-type $Bi_2Mg(Zn)_{1-x}M_xTa_2O_{9.5-\Delta}$ (M-Cr, Fe) ceramics. *Ceram. Int.* **2023**, *49*, 5496–5509. [CrossRef]
27. Zhuk, N.A.; Kovalenko, S.Y.; Korolev, R.I.; Makeev, B.A.; Krzhizhanovskaya, M.G.; Sivkov, D.V.; Nekipelov, S.V.; Sivkov, V.N.; Yermolina, M.V. Features of Phase Formation of Pyrochlore-type Ceramics $Bi_2Mg(Zn)_{1-x}Ni_xTa_2O_9$. *ACS Omega* **2023**, *8*, 11351–11363. [CrossRef]
28. Nino, J.C.; Lanagan, M.T.; Randall, C.A. Phase formation and reactions in the Bi_2O_3–ZnO–Nb_2O_5–Ag pyrochlore system. *J. Mater. Res.* **2001**, *16*, 1460–1464. [CrossRef]
29. Zanetti, S.M.; da Silva, S.A.; Thim, G.P. A chemical route for the synthesis of cubic bismuth zinc niobate pyrochlore nanopowders. *J. Solid State Chem.* **2004**, *177*, 4546–4551. [CrossRef]
30. Zhuk, N.A.; Makeev, B.A.; Korolev, R.I.; Sivkov, D.N.; Shpynova, A.D. A study of phase evolution of Fe-doped bismuth tantalate pyrochlore. *Ceram. Int.* **2022**, *48*, 31965–31969. [CrossRef]
31. Zhuk, N.A.; Makeev, B.A.; Krzhizhanovskaya, M.G.; Nekipelov, S.V.; Sivkov, D.V.; Badanina, K.A. Features of the Phase Formation of Cr/Mn/Fe/Co/Ni/Cu Codoped Bismuth Niobate Pyrochlore. *Crystals* **2023**, *13*, 1202. [CrossRef]

32. Zhuk, N.A.; Badanina, K.A.; Korolev, R.I.; Makeev, B.A.; Krzhizhanovskaya, M.G.; Kharton, V.V. Phase Formation of Co and Cr Co-Doped Bismuth Niobate with Pyrochlore Structure. *Inorganics* **2023**, *11*, 288. [CrossRef]
33. Zhuk, N.A.; Krzhizhanovskaya, M.G.; Koroleva, A.V.; Nekipelov, S.V.; Kharton, V.V.; Sekushin, N.A. Thermal Expansion, XPS Spectra, and Structural and Electrical Properties of a New $Bi_2NiTa_2O_9$ Pyrochlore. *Inorg. Chem.* **2021**, *60*, 4924–4934. [CrossRef] [PubMed]
34. Zhuk, N.A.; Krzhizhanovskaya, M.G.; Sekushin, N.A.; Kharton, V.V.; Koroleva, A.V.; Nekipelov, S.V.; Sivkov, D.V.; Sivkov, V.N.; Makeev, B.A.; Lebedev, A.M.; et al. Novel Ni-Doped Bismuth–Magnesium Tantalate Pyrochlores: Structural and Electrical Properties, Thermal Expansion, X-ray Photoelectron Spectroscopy, and Near-Edge X-ray Absorption Fine Structure Spectra. *ACS Omega* **2021**, *6*, 23262–23273. [CrossRef]
35. Akselrud, L.G.; Grin, Y.N.; Zavalii, P.Y.; Pecharsky, V.K.; Fundamenskii, V.S. CSD-universal program package for single crystal or powder structure data treatment. In Proceedings of the Collected Abstracts of XII European Crystallographic Meeting, Moscow, Russia, 22–29 August 1989.
36. Shannon, R.D. Revised effective ionic radii and systematic studies of interatomic distances in halides and chalcogenides. *Acta Crystallogr. A* **1976**, *32*, 751–767. [CrossRef]
37. Levin, E.M.; Roth, R.S. Polymorphism of bismuth sesquixide. II. Effect of oxide additions on the polymorphism of Bi_2O_3. *J. Res. Natl. Bur. Stand. A Phys. Chem.* **1964**, *68A*, 189–206. [CrossRef]
38. El-Kemary, M.; Nagy, N.; El-Mehasseb, I. Nickel oxide nanoparticles: Synthesis and spectral studies of interactions with glucose. *Mater. Sci. Semicond. Process.* **2013**, *16*, 1747–1752. [CrossRef]
39. Hasnidawani, J.N.; Azlina, H.N.; Norita, H.; Bonnia, N.N.; Ratim, S.; Ali, E.S. Synthesis of ZnO Nanostructures Using Sol-Gel Method. *Procedia Chem.* **2016**, *19*, 211–216. [CrossRef]
40. Pang, L.-X.; Zhou, D.; Wang, H.; Wu, Y.; Guo, J.; Chen, Y.-H. Phase evolution and microwave dielectric properties of Bi_3SbO_7 ceramic. *J. Phys. Chem. Solids* **2011**, *72*, 882–885. [CrossRef]
41. Dutta, D.P. Composites of Sb_2O_4 and Biomass-Derived Mesoporous Disordered Carbon as Versatile Anodes for Sodium-Ion Batteries. *ChemistrySelect* **2020**, *5*, 1846–1857. [CrossRef]
42. Egorysheva, A.; Ellert, O.; Zubavichus, Y.; Gajtko, O.; Efimov, N.; Svetogorov, R.; Murzin, V. New complex bismuth oxides in the Bi_2O_3–NiO–Sb_2O_5 system and their properties. *J. Solid State Chem.* **2015**, *225*, 97–104. [CrossRef]
43. Egorysheva, A.V.; Ellert, O.G.; Gajtko, O.M.; Efimov, N.N.; Svetogorov, R.D.; Zubavichus, Y.V.; Grigorieva, A.V. The Bi_2O_3–Fe_2O_3–Sb_2O_5 system phase diagram refinement, $Bi_3FeSb_2O_{11}$ structure peculiarities and magnetic properties. *J. Solid State Chem.* **2015**, *225*, 278–284. [CrossRef]
44. Sleight, A.W.; Bouchard, R.J. A new cubic $KSbO_3$ derivative structure with interpenetrating networks. Crystal structure of $Bi_3GaSb_2O_{11}$. *Inorg. Chem.* **1973**, *12*, 2314–2316. [CrossRef]
45. Golodukhina, S.V.; Razvorotneva, L.S.; Plukchi, K.R.; Popova, E.F.; Egorysheva, A.V. Successful and not so successful examples of using the citrate method for the synthesis of La and Bi antimonates. *Abstr. All-Russ. Conf. VIII Russ. Rare Earth Day Nizhny Novgorod NNSU IMC RAS* **2024**, *258*, 149–150. Available online: https://iomc.ras.ru/wp-content/uploads/2024/02/rdrz2024_abstracts.pdf (accessed on 26 June 2025).
46. Ramesha, K.; Prakash, A.S.; Sathiya, M.; Madras, G.; Shukla, A.K. Synthesis of new $(Bi, La)_3MSb_2O_{11}$ phases (M = Cr, Mn, Fe) with $KSbO_3$-type structure and their magnetic and photocatalytic properties. *Bull. Mater. Sci.* **2011**, *34*, 271–277. [CrossRef]
47. Evans, I.R.; Shanwen, T.; John, T.; Irvine, S.; Judith Howard, A.K. Synthesis, Crystal Structure, and Oxide Ion Conductivity in $Bi_{4.6}Ca_{1.1}VO_{10.5}$. *Chem. Mater.* **2002**, *14*, 3700–3704. [CrossRef]
48. Badanina, K.A.; Nekipelov, S.V.; Lebedev, A.M.; Zhuk, N.A.; Beznosikov, D.S. Conversion of Cr(III) and Co(III) During the Synthesis of Co/Cr Codoped Bismuth Niobate Pyrochlore According to NEXAFS Data. *J. Sib. Fed. Univ. Math. Phys.* **2024**, *17*, 559–569.
49. Brown, S.; Gupta, H.C.; Alonso, J.A.; Martinez-Lope, M.J. Vibrational spectra and force field calculation of $A_2Mn_2O_7$(A=Y, Dy, Er, Yb) pyrochlores. *J. Raman Spectrosc.* **2003**, *34*, 240–243. [CrossRef]
50. Fischer, M.; Malcherek, T.; Bismayer, U.; Blaha, P.; Schwarz, K. Structure and stability of $Cd_2Nb_2O_7$ and $Cd_2Ta_2O_7$ explored by ab initio calculations. *Phys. Rev. B* **2008**, *78*, 014108. [CrossRef]
51. Patterson, C.H. First-principles calculation of the structure and dielectric properties of $Bi_2Ti_2O_7$. *Phys. Rev. B* **2010**, *82*, 155103. [CrossRef]
52. Krayzman, V.; Levin, I.; Woicik, J.C. Local structure of displacively disordered pyrochlore dielectrics. *Chem. Mater.* **2007**, *19*, 932–936. [CrossRef]
53. Jana, Y.M.; Nand, S.; Gupta, H.C. Lattice dynamics and force constant calculation for the Raman and infra-red wave numbers of cubic bismuth-based pyrochlore compounds. *J. Mol. Struct.* **2018**, *1154*, 463–468. [CrossRef]
54. Sudheendran, K.; Raju, K.C.J.; Singh, M.K.; Katiyar, R.S. Microwave dielectric and Raman scattering studies on bismuth zinc niobate thin films. *J. Appl. Phys.* **2008**, *104*, 104104. [CrossRef]

55. Gupta, H.C.; Brown, S.; Rani, N.; Gohel, V.B. Lattice dynamic investigation of the zone center wavenumbers of the cubic $A_2Ti_2O_7$ pyrochlores. *J. Raman Spectrosc.* **2001**, *32*, 41–44. [CrossRef]
56. Arenas, D.J.; Gasparov, L.V.; Qiu, W.; Nino, J.C.; Patterson, C.H.; Tanner, D.B. Raman study of phonon modes in bismuth pyrochlores. *Phys. Rev. B Condens. Matter Mater. Phys.* **2010**, *82*, 214302. [CrossRef]
57. Chen, M.; Tanner, D.B.; Nino, J.C. Infrared study of the phonon modes in bismuth pyrochlores. *Phys. Rev. B* **2005**, *72*, 54303. [CrossRef]

Disclaimer/Publisher's Note: The statements, opinions and data contained in all publications are solely those of the individual author(s) and contributor(s) and not of MDPI and/or the editor(s). MDPI and/or the editor(s) disclaim responsibility for any injury to people or property resulting from any ideas, methods, instructions or products referred to in the content.